

Enhanced angular resolution from multiply scattered waves

Clifford J Nolan¹, Margaret Cheney², Thomas Dowling¹
and Romina Gaburro¹

¹ Department of Mathematics and Statistics, University of Limerick, Castletroy,
Republic of Ireland

² Department of Mathematical Sciences, Rensselaer Polytechnic Institute, Troy, NY 12180, USA

E-mail: clifford.nolan@ul.ie, cheney@rpi.edu, thomas.dowling@ul.ie and romina.gaburro@ul.ie

Received 11 April 2006, in final form 20 July 2006

Published 18 September 2006

Online at stacks.iop.org/IP/22/1817

Abstract

Multiply scattered waves are often neglected in imaging methods, largely because of the inability of standard algorithms to deal with the associated non-linear models. This paper shows that by incorporating a known environment into the background model, we not only retain the benefits of imaging techniques based on linear models, but also obtain different views of the target scatterer. The net result is an enhanced angular resolution of the target to be imaged. We carry out our analysis in the context of high-frequency radar imaging, in which a steerable beam from a moving platform is used to produce an image of a region on the earth's surface (the target scatterers being buildings, etc). We consider the case where the target we want to image is situated in the vicinity of an *a priori* known reflecting wall. This is one of the simplest possible multipathing environments for the scatterer, and in the case when the illuminating beam is narrow enough to isolate different scattering paths, we will show that the imaging process achieves enhanced angular resolution. Although we carry out our analysis here in the context of radar, our technique is general enough that it can be adapted to many imaging modalities, such as acoustics, ultrasound, elasticity, etc. The extension of the method to other more complicated environments is also possible.

1. Introduction

Imaging modalities such as reflection seismology, medical ultrasound imaging, and radar imaging involve reconstructing a scatterer from reflected waves. In such problems, it is common to use the *Born* approximation, which is a single- (weak-) scattering approximation. In other words, one assumes that after a wave is emitted from a source, it scatters from the target to be imaged only once and then returns to the detector. In reality, however, waves can

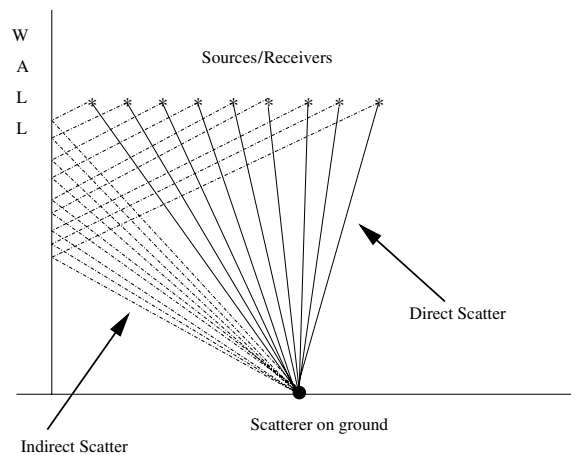


Figure 1. Increased angles of the view of the target scatterer on the ground through the use of the multiply scattered waves from the wall. The wave may scatter off the wall on the way down only, or on the way up only, or on both ways. Or indeed, the wave may not scatter from the wall at all and just scatter directly to and from the target. We neglect diffracted waves from the corners/edges of the wall.

scatter several times before returning to the detector. For example, the wave may scatter from other unknown targets, or they may scatter from an *a priori* known scatterer, such as a nearby wall in the context of radar imaging in an urban setting. In this paper, we incorporate a wall into the background model and calculate the corresponding background Green's function. Based on this Green's function, we produce an image of the region of interest, using the backprojection technique described in [4].

Related work is [1, 2], which also incorporate information about scatterers in the environment. This earlier work deals with reconstruction using a finite number of discrete frequencies, and uses a Hilbert-space approach for the reconstruction. Natterer and his group at Münster have also studied related questions in work that is currently unpublished. Our approach complements these works because we operate in the time domain and also use microlocal analysis to point out artefacts which can arise (unless avoidance measures are taken), and we illustrate these in our numerical simulations.

This approach was used in [12], which investigated imaging in the presence of a known point scatterer in proximity to the target to be imaged. In [12], it was not necessary to separate the data corresponding to different scattering paths; however, the imaging technique was able to focus only the part of the data for which either the incident wave or the scattered wave propagated along a direct path between the target and sensor. If the imaging method is extended to handle more severe multipath scattering, then one can obtain a better-resolved image at the expense of introducing artefacts.

All this previous work is consistent with the results of this paper in finding that, for limited-aperture problems, the resolution is improved when multipath scattering is correctly taken into account. This is based on the observation that multipath scattering provides more views of the target than can be obtained from direct scattering (see figure 1).

In our measurement scenarios, the location of the source of wave energy is also the location at which the scattered wave is measured (by the same sensor). That is to say, our sources and receivers of the electromagnetic waves are coincident.

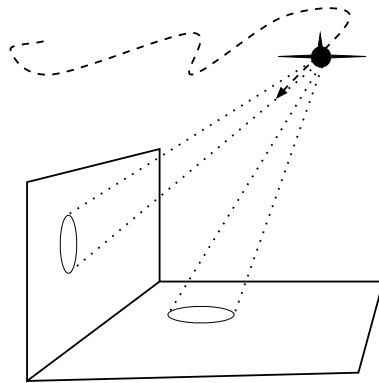


Figure 2. Data acquisition.

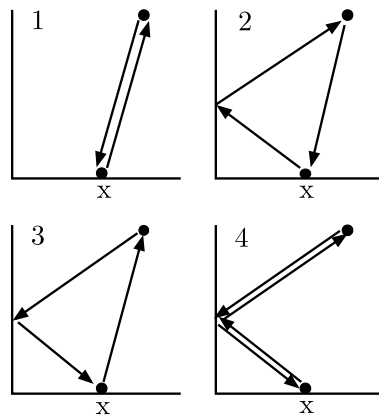


Figure 3. In path 1, the wave scatters directly to and from the target. In path 2, the wave scatters from the target to the wall and back to the receiver. In path 3, the wave scatters from the wall to the target and back to the receiver. Finally, in path 4, the wave scatters to the wall to the target and back to the wall again before returning to the receiver.

Figure 2 shows the geometry we consider here: the sensor can travel on any smooth path, and the sensor can direct narrow beams in a variety of directions. In this case, the sensor might be transmitting a narrow beam towards the wall and forming a receive beam to record the resulting waves that scatter from targets on the ground.

Figure 3 shows four possible propagation paths, which we will incorporate into our imaging. Waves could of course bounce multiple times between the wall and target, but we will neglect all waves that interact with the target more than once. The work in this paper applies to a system with a narrow beam whose direction can be controlled to isolate the data from the different paths. If our radar system cannot do this, we will obtain artefacts.

The outline of the paper is as follows. In section 2, we develop a scattering model for scattered waves in the presence of a vertical wall. This is achieved through the use of the method of images. In section 3, we briefly review how to carry out imaging from the data corresponding to paths 1 and 4. In the subsequent subsection, we show how we can bootstrap the latter method to image from the data corresponding to paths 2 and 3.

In section 4, we present some numerical simulations to illustrate our ideas and show that the method works. We also observe in the numerical section that artefacts develop if the radar does not direct its beam to appropriate locations. The theory needed to explain this involves microlocal analysis [5, 7]. In order to keep this paper self-contained and more accessible, we omit such details and will instead publish a study of this in the near future.

2. The mathematical model

2.1. A model for the wave propagation

We consider the simple scalar wave equation to model the wave propagation. Although the radar waves are electromagnetic, and therefore vectorial, we will assume that between the antenna and the ground, the medium is homogeneous, and that therefore, to a good approximation, each component (denoted by u below) of the electric field satisfies the same scalar wave equation

$$\left(\nabla^2 - \frac{1}{c^2(\mathbf{x})} \partial_t^2 \right) u(t, \mathbf{x}) = f, \quad (1)$$

with perhaps different sources (f) on the right-hand sides of these scalar wave equations. For a more in-depth discussion of the model that follows below, see [4, 6, 8, 9], where the function c is the wave propagation speed. Equation (1) is commonly used in SAR (synthetic aperture radar), and it also represents a good model for sonar and ultrasound in similar circumstances.

Assumption 2.1. *We assume that the target is well separated from the region where the sensors are located and that below the sensors the wave speed c in the wave equation (1) can be written as $c^{-2}(\mathbf{x}) = c_0^{-2} + \tilde{V}(\mathbf{x})$, where c_0 is a constant (for radar applications c_0 is the speed of light in a vacuum) and $\tilde{V}(\mathbf{x})$ is an unknown perturbation that we wish to recover from the scattered waves.*

Assumption 2.2. *We assume that the target to be imaged (encoded in $\tilde{V}(\mathbf{x})$) is a priori known to lie on the ground and on the right-hand side ($x_1 > 0$) of a vertical wall. We assume that the ground is flat, so if we denote by (x_1, x_2, x_3) the Cartesian coordinates in \mathbb{R}^3 , then the ground is $\mathbb{R}^2 = \{(x_1, x_2, 0) \mid x_i \in \mathbb{R}, i = 1, 2\} \subseteq \mathbb{R}^3$. We assume that the perturbation is of the form $\tilde{V}(\mathbf{x}) = V(x_1, x_2)\delta(x_3)$, where V is the ground reflectivity function.*

The vertical wall can be taken for simplicity as the infinite vertical plane $x_1 = 0$, so we can identify the area to be imaged by the set $\mathbb{R}_+^2 = \{(x_1, x_2, 0) \mid x_i \in \mathbb{R}, i = 1, 2, x_1 > 0\}$.

While the assumption of an infinite wall is convenient for the subsequent analysis, in reality the wall is finite and we therefore can only legitimately image that part of the ground visible from multiple reflections from the actual wall (rather than the idealized one). However, we can easily account for this by modifying the antenna beam patterns below to be zero when they illuminate extraneous parts of the wall. Therefore, these data cannot contribute to the image and there is no problem with our idealized assumption. Also, if the location of the wall is unknown, we envisage an extension of this work whereby it is first estimated using directly scattered waves. We do not attempt to develop this idea here. We also neglect the diffracted field from the corners/edges of the wall. We justify this on the basis that the diffracted waves would normally be significantly weaker than the specular contribution accounted for here.

Assumption 2.3. *The boundary condition at the wall is the Dirichlet boundary condition.*

$$u(t, \mathbf{x}) \Big|_{x_1=0} = 0. \quad (2)$$

The form of the boundary condition is not crucial, and we chose the Dirichlet condition for simplicity. Other boundary conditions can be treated with methods similar to those below. Handling a wall of unknown material might require an additional optimization step in the imaging process to determine the appropriate wall reflection parameter.

2.2. Wave propagation in the vicinity of a vertical wall

Green's function G is required to satisfy

$$\begin{cases} \left(\nabla^2 - \frac{1}{c_0^2} \partial_t^2 \right) g = -\delta(t) \delta(\mathbf{x} - \mathbf{y}^0), & \text{for } x_1 > 0 \\ g|_{x_1=0} = 0 \\ g|_{t \leq 0} = 0 \end{cases}$$

with the latter condition ensuring causality.

Definition 2.1. For any point $\mathbf{x} = (x_1, x_2, x_3)$, we denote by $\tilde{\mathbf{x}}$ its reflection with respect to the wall, $x_1 = 0$, i.e.,

$$\tilde{\mathbf{x}} = (-x_1, x_2, x_3). \quad (3)$$

By the method of images, we can write g explicitly as

$$g(t, \mathbf{x} - \mathbf{y}) = \frac{\delta\left(t - \frac{|\mathbf{x} - \mathbf{y}|}{c_0}\right)}{4\pi |\mathbf{x} - \mathbf{y}|} - \frac{\delta\left(t - \frac{|\mathbf{x} - \tilde{\mathbf{y}}|}{c_0}\right)}{4\pi |\mathbf{x} - \tilde{\mathbf{y}}|}, \quad (4)$$

where \mathbf{y} and $\tilde{\mathbf{y}}$ are the locations of the real and virtual point sources, respectively.

2.3. A linearized scattering model

For a sensor located at \mathbf{y} , a derivation similar to that of [4, 8] shows that the measured signal can be written as follows:

$$\begin{aligned} S(t, \mathbf{y}; j_s, j_r) &\approx \int \frac{e^{-i\omega(t-2|z-\mathbf{y}|/c_0)}}{(4\pi)^2 |z-\mathbf{y}|^2} \omega^2 P(\omega) j_s(\omega \widehat{(\mathbf{z}-\mathbf{y})}, \mathbf{y}) j_r(\omega \widehat{(\mathbf{z}-\mathbf{y})}, \mathbf{y}) V(z) d\omega dz \\ &\quad - \int \frac{e^{-i\omega(t-(|z-\mathbf{y}|+|z-\tilde{\mathbf{y}}|)/c_0)}}{(4\pi)^2 |z-\mathbf{y}||z-\tilde{\mathbf{y}}|} \omega^2 P(\omega) j_s(\omega \widehat{(\mathbf{z}-\tilde{\mathbf{y}})}, \tilde{\mathbf{y}}) j_r(\omega \widehat{(\mathbf{z}-\mathbf{y})}, \mathbf{y}) V(z) d\omega dz \\ &\quad - \int \frac{e^{-i\omega(t-(|z-\mathbf{y}|+|z-\tilde{\mathbf{y}}|)/c_0)}}{(4\pi)^2 |z-\mathbf{y}||z-\tilde{\mathbf{y}}|} \omega^2 P(\omega) j_s(\omega \widehat{(\mathbf{z}-\mathbf{y})}, \mathbf{y}) j_r(\omega \widehat{(\mathbf{z}-\tilde{\mathbf{y}})}, \tilde{\mathbf{y}}) V(z) d\omega dz \\ &\quad + \int \frac{e^{-i\omega(t-2|z-\tilde{\mathbf{y}}|/c_0)}}{(4\pi)^2 |z-\tilde{\mathbf{y}}|^2} \omega^2 P(\omega) j_s(\omega \widehat{(\mathbf{z}-\tilde{\mathbf{y}})}, \tilde{\mathbf{y}}) j_r(\omega \widehat{(\mathbf{z}-\tilde{\mathbf{y}})}, \tilde{\mathbf{y}}) V(z) d\omega dz \end{aligned}$$

where j_r and j_s denote receiver and source antenna beam patterns, respectively, and $p(\omega)$ denotes the Fourier transform of the transmitted waveform $p(t)$. We see that the first term corresponds to path 1, the second to path 2, etc.

3. Imaging

The idealized inverse problems consist in determining V from knowledge of $S(t, \mathbf{y})$ for an interval of time, $t \in [0, T]$ and for \mathbf{y} on the known curve

$$\Gamma_+ := \{\Gamma_+(s) | s^{\min} < s < s^{\max}\}.$$

We also define

$$\Gamma_- := \{\Gamma_-(s) | s^{\min} < s < s^{\max}\}$$

which is the mirror image of the curve Γ_+ .

It is well known that data with abrupt end points tend to cause artefacts in imaging algorithms; in this case, to avoid artefacts in the image due to the abrupt edges of Γ_+ and time, we multiply the data by a *mute* function $m(s, t)$, which is a smooth cut-off function with compact support:

$$\text{supp}(m) \subseteq [s^{\min}, s^{\max}] \times [0, T].$$

We denote the *forward map* from scene V to data $d = mS$ by F , so that

$$\begin{aligned} FV(s, t; j_s, j_r) &= \int e^{-i\omega(t-2|z-\Gamma_+(s)|/c_0)} A_1(z, s, t, \omega; j_s, j_r) V(z) d\omega dz \\ &\quad - \int e^{-i\omega(t-(|z-\Gamma_+(s)|+|z-\Gamma_-(s)|)/c_0)} A_2(z, s, t, \omega; j_s, j_r) V(z) d\omega dz \\ &\quad + \int e^{-i\omega(t-(|z-\Gamma_+(s)|+|z-\Gamma_-(s)|)/c_0)} A_3(z, s, t, \omega; j_s, j_r) V(z) d\omega dz \\ &\quad + \int e^{-i\omega(t-2|z-\Gamma_-(s)|/c_0)} A_4(z, s, t, \omega; j_s, j_r) V(z) d\omega dz \\ &:= [F_1 + F_2 + F_3 + F_4]V(s, t; j_s, j_r), \end{aligned} \quad (5)$$

where the amplitudes include the beam patterns for transmission and reception, the transmitted waveform, the $1/r^2$ geometrical spreading factors and the mute function. We see that the term F_1 corresponds to direct scattering, F_2 corresponds to path 2, etc.

We make the following assumption.

Assumption 3.1. For any $j = 1, 2, 3, 4$, the amplitude A_j satisfies

$$\sup_{(s,t,x) \in K} \left| \partial_\omega^\alpha \partial_s^\beta \partial_t^\delta \partial_x^\rho A_j(\mathbf{x}, s, t, \omega; j_s, j_r) \right| \leq C_{K,\alpha,\beta,\delta,\rho}^j (1 + \omega^2)^{(2-|\alpha|)/2}, \quad (6)$$

where K is any compact set and $\alpha, \beta, \delta, \rho$ are arbitrary multi-indices of the appropriate dimension.

Assumption 3.1 is valid, for example, when the waveform p is approximately a delta function and the antenna is sufficiently broadband (see [1] for further discussion of this). We note that, under assumption 3.1, the forward operators F_j are so-called Fourier integral operators (FIOs) [5], for $j = 1, 2, 3, 4$. These are well-studied operators with many useful properties that we can utilize. In particular, our imaging scheme and artefact prediction are based on considerations from FIO theory (which is part of microlocal analysis).

3.1. Data decomposition

By choosing the beam patterns j_s, j_r appropriately, we can isolate separate data sets corresponding to the different paths shown in figure 2. In particular, we choose j_s^i and j_r^i so that $A_k(z, s, t, \omega; j_s^i, j_r^i) \approx 0$ for $i \neq k$ but $A_i(z, s, t, \omega; j_s^i, j_r^i) \neq 0$. By this means, we obtain data d_i corresponding to separate paths:

$$d_i(s, t) = FV(s, t; j_s^i, j_r^i) \approx F_i V(s, t; j_w^i, j_r^i), \quad i = 1, 2, 3, 4. \quad (7)$$

Figure 4 illustrates the range of beam directions for j_s, j_r to obtain data set d_2 , for example.

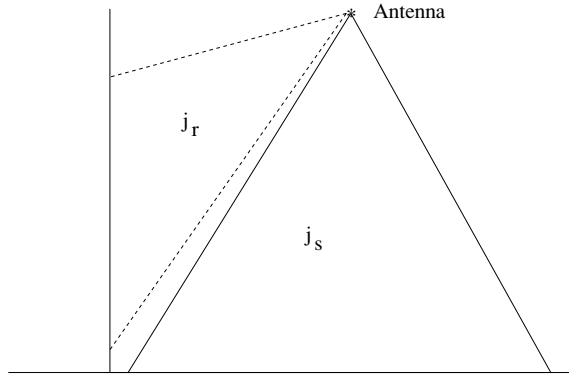


Figure 4. Illustration of how data set d_2 can be isolated by choice of the beam patterns.

Assumption 3.2. *We neglect the antenna side-lobes. We also neglect diffraction effects from the edge of the wall. We assume, moreover, that the beam can be swept so rapidly that data for all paths are available for each position s along the flight path.*

In particular, this assumption requires that we avoid illuminating the wall–ground interface.

If diffraction effects are present, it is possible that some of them could be treated by the method of [12]; we leave this for future research.

3.2. Image formation from individual data sets

Our goal is to reconstruct an image of the scatterers. This is usually done by applying a filtered adjoint of the scattering operator to the data. This procedure goes by various names in different communities; e.g., ‘matched filtering’ (radar), ‘migration’ (geophysics), ‘filtered backprojection’ (tomography), etc.

In our case, we apply to the data set d_i a filtered adjoint: the imaging operator has the same phase as the adjoint F_i^* of F_i , with the filter to be chosen later. The appropriate images $I_i(x)$ at a point x are therefore

$$I_1(\mathbf{x}) := \int e^{i\omega(t-2|\mathbf{x}-\Gamma_+(s)|/c_0)} a_1(\mathbf{x}, s, t, \omega) d_1(s, t) d\omega ds dt, \quad (8)$$

$$I_2(\mathbf{x}) := \int e^{i\omega(t-(|\mathbf{x}-\Gamma_+(s)|+|\mathbf{x}-\Gamma_-(s)|)/c_0)} a_2(\mathbf{x}, s, t, \omega) d_2(s, t) d\omega ds dt, \quad (9)$$

$$I_3(\mathbf{x}) := \int e^{i\omega(t-(|\mathbf{x}-\Gamma_+(s)|+|\mathbf{x}-\Gamma_-(s)|)/c_0)} a_3(\mathbf{x}, s, t, \omega) d_3(s, t) d\omega ds dt, \quad (10)$$

$$I_4(\mathbf{x}) := \int e^{i\omega(t-2|\mathbf{x}-\Gamma_-(s)|/c_0)} a_4(\mathbf{x}, s, t, \omega) d_4(s, t) d\omega ds dt,$$

where the amplitudes a_i , $i = 1, 2, 3, 4$ are to be chosen later.

3.3. Imaging data sets 1 and 4

We will deal with the image I_1 first because this case has already been investigated in [4]. We will briefly review the analysis of this image here again, as we will build on it for analysis of the remaining images.

Into (8) we substitute (7) for $i = 1$. This results in

$$I_1(\mathbf{x}) = \int e^{i\phi(s,t,\mathbf{x},z,\omega,\tilde{\omega})} b_1(s, t, \mathbf{x}, z, \omega, \tilde{\omega}) V(z) dz d\omega d\tilde{\omega} d\mathbf{x} ds dt \tag{11}$$

where

$$\begin{aligned} \phi_1(s, t, \mathbf{x}, z, \omega, \tilde{\omega}) &= t(\omega - \tilde{\omega}) + 2(\omega|z - \Gamma_+(s)| - \tilde{\omega}|\mathbf{x} - \Gamma_+(s)|)/c_0 \\ b_1(s, t, \mathbf{x}, z, \omega, \tilde{\omega}) &= a_1(\mathbf{x}, s, t, \omega) A_1(z, s, t, \tilde{\omega}). \end{aligned} \tag{12}$$

Performing a leading-order stationary-phase calculation in the variables $(\tilde{\omega}, t)$ amounts to replacing the phase and amplitude by

$$\phi_1(s, \mathbf{x}, z, \omega) = 2\omega(|z - \Gamma_+(s)| - |\mathbf{x} - \Gamma_+(s)|)/c_0 \tag{13}$$

$$b_1(s, \mathbf{x}, z, \omega) = a_1(\mathbf{x}, s, 2|\mathbf{x} - \Gamma_+(s)|/c_0, \omega) A_1(z, s, 2|\mathbf{x} - \Gamma_+(s)|/c_0, \omega), \tag{14}$$

respectively.

We see therefore that ϕ_1 can be replaced by

$$\phi_1(s, \mathbf{x}, z, \omega) = f_1(z, s, \omega) - f_1(\mathbf{x}, s, \omega) \tag{15}$$

where

$$f_1(z, s, \omega) = 2\omega|z - \Gamma_+(s)|/c_0. \tag{16}$$

The phase (15) has two critical points, namely $\mathbf{x} = z$ and $\mathbf{x} = \tilde{z}$, where \tilde{z} is the reflection of z across the projection of the line tangent to the flight path. This extra critical point leads to a classic artefact which manifests itself as a ghost image of the target, reflected symmetrically about the flight track [4, 13, 14]. This artefact can be avoided by using a side-looking radar system; in the analysis below we restrict ourselves to such systems.

Using Taylor's theorem, we obtain

$$\begin{aligned} \phi_1(s, \mathbf{x}, z, \omega) &= (\mathbf{x} - z) \cdot \Xi(z, \mathbf{x}, s, \omega) \\ \Xi(z, \mathbf{x}, s, \omega) &:= -\frac{2\omega}{c_0} \int_0^1 \nabla_z f_1((1 - \lambda)\mathbf{x} + \lambda z, s, \omega) d\lambda. \end{aligned} \tag{17}$$

Consequently,

$$I_1(\mathbf{x}) = \int e^{i(\mathbf{x}-z) \cdot \Xi(z,\mathbf{x},s,\omega)} b_1(s, \mathbf{x}, z, \omega) V(z) dz d\omega ds. \tag{18}$$

Remark 3.1. By a stationary phase argument, we can assume without loss of generality that the amplitude b_1 need only be non-zero near $z = \mathbf{x}$. Indeed, the error made by violating this assumption is an integral whose integrand is rapidly decaying in ω ; hence this error term is infinitely smooth. We are willing to ignore such errors in our approximation; we instead concentrate on recovery of singularities in V .

Explicitly, we use the change-of-variables mapping

$$\psi_1 : (s, \omega) \mapsto \boldsymbol{\xi} := \Xi(\mathbf{x}, \mathbf{x}, s, \omega) = -2(\omega/c_0) (\widehat{R}_x^+)_H \tag{19}$$

where

$$R_x^+ = \mathbf{x} - \Gamma_+(s) \tag{20}$$

and the subscript H stands for the horizontal component (first two components). For z, \mathbf{x} fixed, we observe (see [4] for details) that the map ψ_1 is a diffeomorphism, provided that \mathbf{x} is not on the projection of the line tangent to the flight path. The fact that ψ_1 is a diffeomorphism at every illuminated point means that the change of variables (19) can be made at every such point.

After the change of variable (19), we obtain

$$I_1(x) \sim \int e^{i(x-z)\cdot\xi} \tilde{b}_1(x, z, \xi) V(z) dz d\omega ds \quad (21)$$

where \tilde{b}_1 incorporates a Jacobian factor from the change of variable. It is possible to choose the original amplitude a_1 of (8) so that \tilde{b}_1 is equal to $(2\pi)^{-2}$ for those values of (z, ξ) belonging to a certain open set. Then (21) looks like a filtered Fourier inversion of the Fourier transform of V . The filter arises from the fact that not all Fourier directions ξ are present.

From microlocal analysis, we find that the above calculations show that we have obtained in (21) an image which captures those singularities of V that are visible from the side-looking data (which is all that can be expected). In other words, (21) acts roughly like Fourier inversion over as large a solid angle and as many frequencies as possible.

Similar analysis applies to data set 4 because it is basically the same situation with the source position now changed to the virtual source location.

3.4. Imaging data sets 2 and 3

Next we come to the data corresponding to paths 2 and 3 and we will carry out the analysis of the weighted backprojected image for the data d_2, d_3 in the same way. Since paths 2 and 3 have the same phase function, we need only carry out the analysis for path 2, the analysis for path 3 being very similar.

Remark 3.2. The situation now under consideration is equivalent to the ‘common midpoint’ geometry for data acquisition in geophysics. The imaging for this path was previously considered abstractly (non-explicitly) in [11]. In the latter paper, there was a ‘traveltime injectivity’ condition that needs to be valid in order to avoid artefacts. The consequences of violating this condition will be analysed using microlocal analysis elsewhere but for now, suffice it to say that there can be an additional ghost image (artefact) of the target and this artefact is positioned symmetrically about the wall. This is borne out in the numerical simulations.

The imaging analysis is identical to that of I_1 , up to (19), with f_1 now being replaced by

$$f_1(z, s, \omega) = \omega(|z - \Gamma_-(s)| + |z - \Gamma_+(s)|)/c_0 \quad (22)$$

and (19) being replaced by

$$\Xi(x, x, s, \omega) = -(\omega/c_0)(\widehat{R}_x^+ + \widehat{R}_x^-)_H \quad (23)$$

where

$$R_x^- = x - \Gamma_-(s). \quad (24)$$

We make the change of variables

$$\psi_2 : (s, \omega) \rightarrow -(\omega/c_0)(\widehat{R}_x^+ + \widehat{R}_x^-)_H. \quad (25)$$

The legitimacy of this change of variables is determined by an investigation of the Jacobian $D\psi_2$ of the mapping ψ_2 , which is proportional (see [4]) to the 2×2 matrix

$$\left[-(\widehat{R}_x^+ + \widehat{R}_x^-)_H (P_+ \dot{\Gamma}_+(s) + P_- \dot{\Gamma}_-(s))_H \right] \quad (26)$$

where the dot denotes differentiation with respect to s and where P_+ is the operator

$$P_+ v = \frac{v - \widehat{R}_x^+ (\widehat{R}_x^+ \cdot v)}{|\widehat{R}_x^+|} \quad (27)$$

and P_- is defined similarly using \widehat{R}_x^- instead of \widehat{R}_x^+ . The operators P_+ and P_- project a vector onto the plane perpendicular to \widehat{R}_x^+ and \widehat{R}_x^- , respectively.

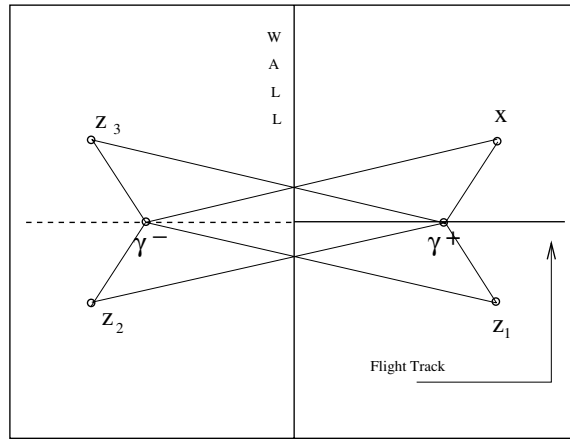


Figure 5. Illustration of the artefacts that can arise in experiments 2 and 3 when the flight track is perpendicular to the wall, as shown.

The set of points x where the Jacobian (26) is singular is generically a (possibly non-smooth) one-dimensional curve. The region illuminated by the antenna should (i) not illuminate in a neighbourhood of this curve and (ii) ensure that this region contains no critical points other than those for which $z = x$. (See the critical equations (29, 30) below). Under these conditions, we can make the change of variable ψ_2 , and once again obtain artefact-free images I_2, I_3 , as we did for I_1, I_4 . Analytically calculating the set of ‘bad’ points x that should not be illuminated is not easy, except in a few cases. However, computing these bad points can easily be done numerically during the backprojection step. One of the cases that can be worked out analytically is when the velocity $\dot{\Gamma}_+(s)$ is perpendicular to the wall. In this case, points on the wall ($x_1 = 0$) must be avoided: for such points, both columns of (26) are pointing in the x_2 direction. Similarly points along the projected flight track must be avoided. To avoid illuminating more than one critical point, we should only illuminate on one side of the wall and one side of the flight track.

If the antenna does illuminate points for which (26) is singular, we may have artefacts. To see this, we apply the method of stationary phase to I_2 . The phase ϕ_2 of I_2 is

$$\phi_2(z, s, \omega) = f_1(z, s, \omega) - f_1(x, s, \omega), \tag{28}$$

where f_1 is given by (22). The stationary phase conditions are

$$|z - \Gamma_+(s)| + |z - \Gamma_-(s)| = |x - \Gamma_+(s)| + |x - \Gamma_-(s)| \tag{29}$$

$$z - \widehat{\Gamma}_+(s) \cdot \dot{\Gamma}_+(s) + z - \widehat{\Gamma}_-(s) \cdot \dot{\Gamma}_-(s) = x - \widehat{\Gamma}_+(s) \cdot \dot{\Gamma}_+(s) + x - \widehat{\Gamma}_-(s) \cdot \dot{\Gamma}_-(s). \tag{30}$$

When the velocity is perpendicular to the wall, for example, it is easy to verify that the following values of z satisfy the stationary conditions: (i) $z = x$, (ii) $z =$ mirror image of x across the (projection of the) flight track, (iii) $z =$ mirror image of x across the wall and (iv) $z =$ mirror image of (ii) across the wall (see figure 5). A similar simple argument applies when the velocity is parallel to the wall, leading to an artefact that is mirrored across the wall. This explains the artefacts in figures 10 and 14 of the next section.

If we drop the illumination restrictions (side-looking, etc), it turns out that ψ_2 is not injective and artefacts will arise in the backprojected image. The analysis of these artefacts requires more sophisticated microlocal machinery and consequently will be analysed elsewhere.

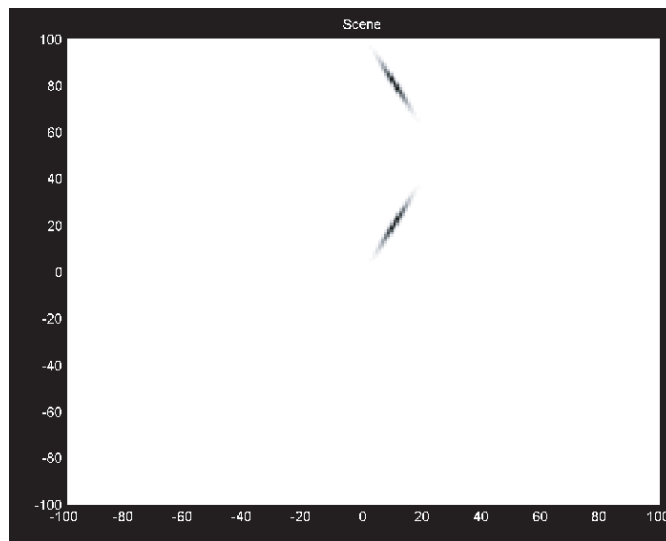


Figure 6. Pair of target scatterers to be imaged.

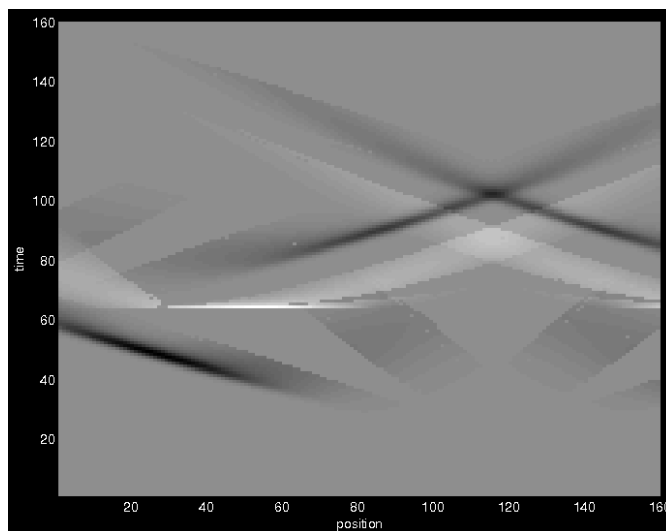


Figure 7. Complete data set corresponding to above targets. The flight track was $\{(30, s) : s \in [0, 70]\}$. The sampling in 's' was 0.5 m. The time along the vertical axis is scaled by 6×10^{-5} s. The frequency content of the isotropic source used was 100–200 Mhz.

4. Numerical experiments

In all the following numerical experiments, the wall is located at $x_1 = 0$. It is depicted by a solid black line. This is not to be confused with another shorter black line, which depicts the projection of the flight track (flying at a height of 8 km) onto the ground. The frequency band of the transmitted waveform was 100–200 MHz.

Figure 6 shows the first scene to be imaged: a pair of oppositely slanting reflectors. We generated data for each of the paths 1, 2, 3, 4 separately. Figure 7 shows the synthetic data

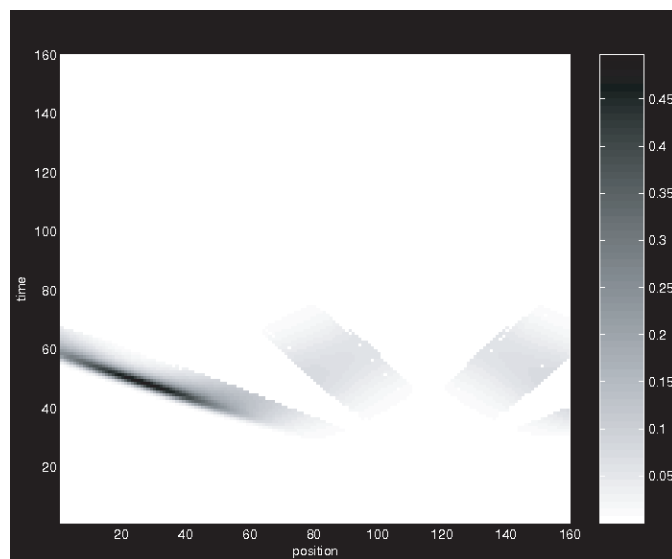


Figure 8. Data set d_1 , showing the visibility of the lower reflector and the second reflector just about coming into view by the end of the time/flight tracks intervals.

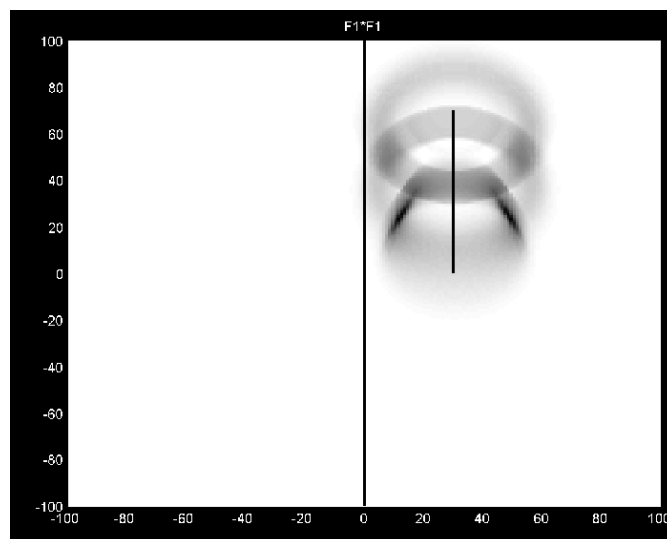


Figure 9. Reconstruction from data set d_1 . The long black vertical line marks the intersection of the vertical wall with the ground. The short black vertical line marks the projection of the flight track on the ground.

summed over all four paths, as would be obtained from an isotropic antenna. The data for paths 2 and 3 coincide (as they have the same traveltimes). Figure 8 shows the individual data set d_1 , which would be obtained from a narrow antenna beam illuminating only the ground and not the wall. Figures 9–11 show the reconstructions based on data sets d_1, d_2 and d_3, d_4 respectively. The lower reflector tilts so that it is easily visible in data set d_1 , whereas the upper reflector is tilted to be nearly invisible from direct-path scattering. Consequently, in

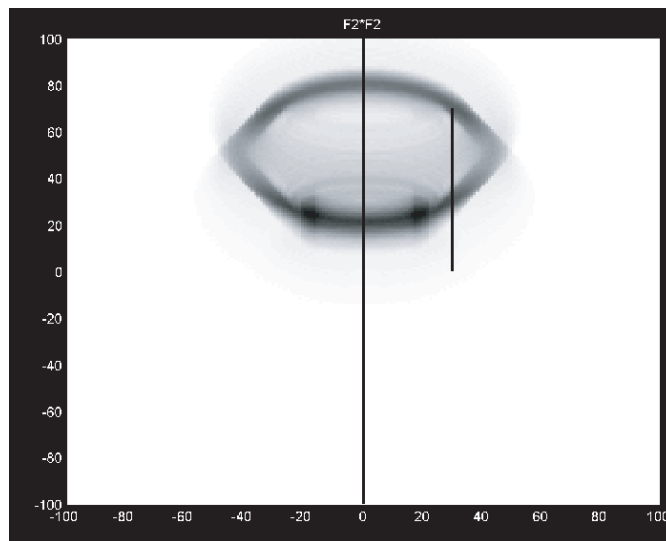


Figure 10. Reconstruction from data sets d_2, d_3 . See comments in text explaining how this reconstruction can be improved by flying a different flight track.

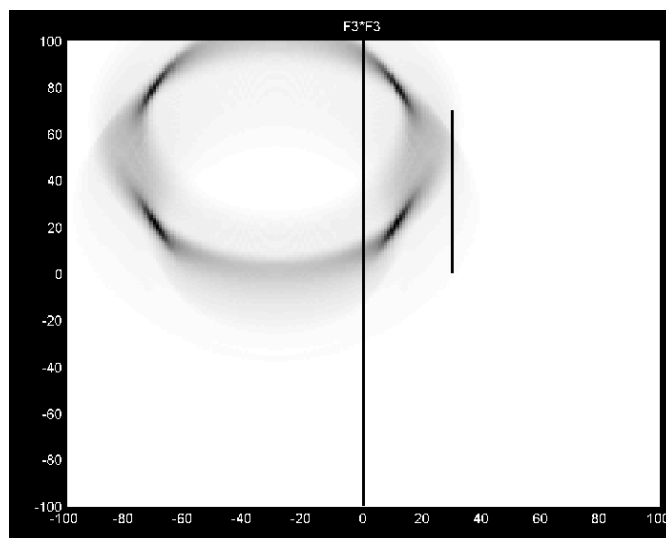


Figure 11. Reconstruction from data set d_4 .

figure 9, the lower reflector is well imaged, whereas the upper one is poorly imaged. The upper reflector, however, is visible from multipath bounces: when d_2, d_3 are used with the image formation process (9), we obtain figure 10, in which the image of the upper reflector is improved. A much better image of the upper reflector is obtained from the multipath data d_4 (and the corresponding backprojected image) as seen in figure 11. This is the improvement we expect from using the bounced signal off the wall. (We explain below why d_2, d_3 may afford only a partial improvement, depending on the flight track that is used.) Finally, a coherent sum (figure 12) of all the individual images is the best of all.

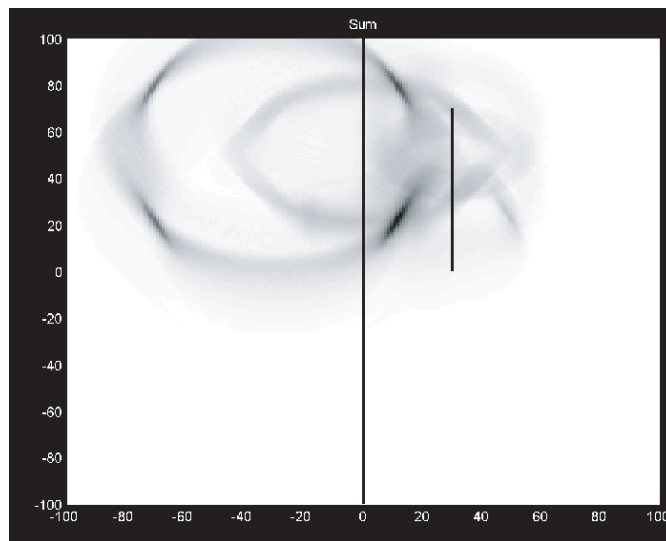


Figure 12. Reconstruction using all data sets.

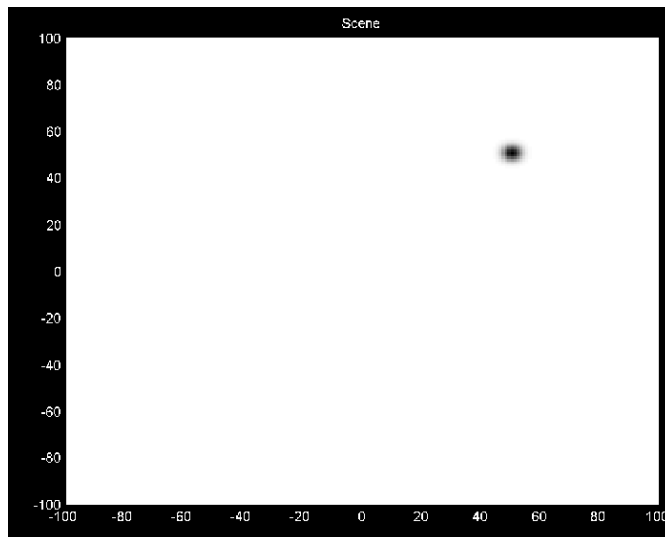


Figure 13. Single scatterer located at (50, 50) to be reconstructed in next figures.

We ran a different set of numerical experiments using the single point-like scatterer seen in figure 13. The point of these experiments is three-fold. First we want to point out a potential shortcoming associated with imaging from data set d_2, d_3 and how it can be improved. Secondly, we will demonstrate new artefacts associated with the backprojected image obtained from d_2 . And thirdly, we will show how to avoid these artefacts by operating a side-looking radar.

For the single point-like scatterer, we used a horizontal flight track, as seen in figure 14. We see that the d_2, d_3 reconstruction of figure 14 is better than its counterpart in figure 10. The reason for this improvement has to do with the intersection of the ellipsoids $t = (|\mathbf{x} - \Gamma_+(s)| + |\mathbf{x} - \Gamma_-(s)|)/c_0$ with the ground, along which the backprojection is

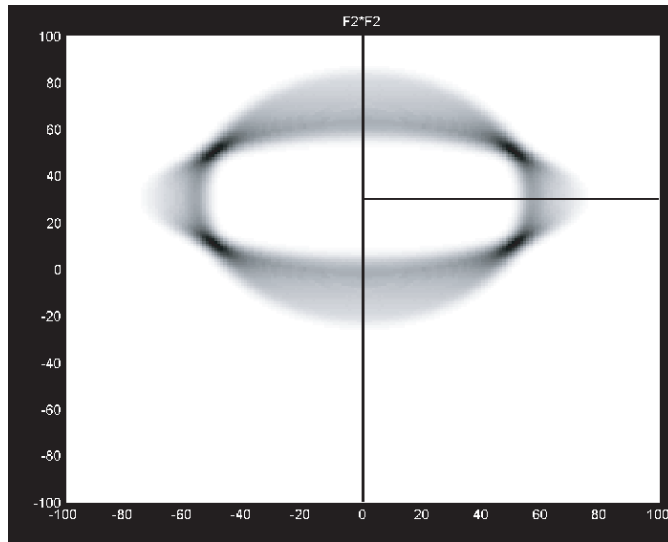


Figure 14. Reconstruction from paths 2 and 3 using a horizontal flight track as shown. Reconstruction is smeared diagonally, and has expected artefacts.

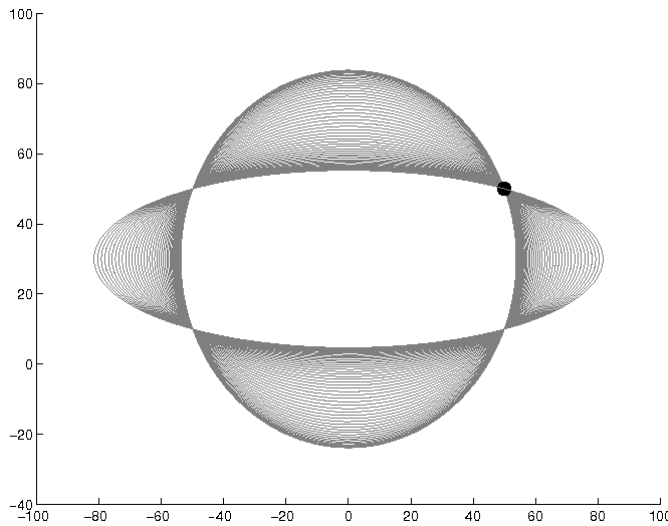


Figure 15. A picture of ellipsoids contributing to the backprojected image in figure 14, i.e., a family of ellipsoids with foci along the flight track and its virtual image. Note that the smearing in figure 14 corresponds to a neighbourhood of the intersecting ellipsoids at (50, 50) and the corresponding artefact locations.

done. For reference, we give the equation of these ellipsoids

$$\frac{4x_1^2(c_0^2t^2/4 - \Gamma_1^+(s)^2)}{c_0^2t^2(c_0^2t^2/4 - \Gamma_1^+(s)^2 - h^2)} + \frac{(x_2 - \Gamma_2^+(s))^2}{c_0^2t^2/4 - \Gamma_1^+(s)^2 - h^2} = 1 \tag{31}$$

where h is the height at which the antenna is flying.

When reconstructing an image at a fixed location, as depicted by the dot in figures 13 and 15, the data coming from various such ellipsoids all contribute to the image. This can be seen

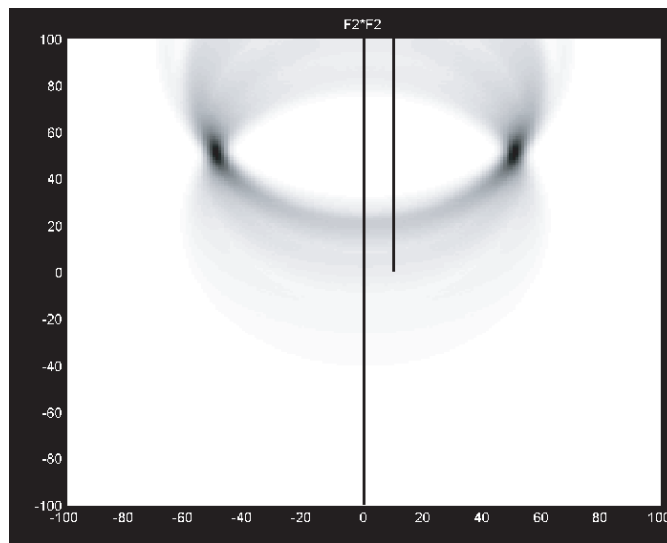


Figure 16. Reconstruction from paths 2 and 3 using a vertical flight track as shown. Reconstruction is smeared approximately vertically, and has expected artefacts.

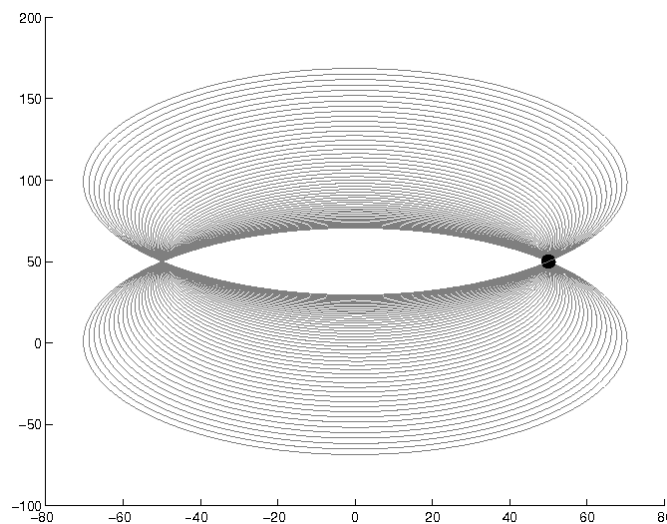


Figure 17. A picture of ellipsoids contributing to the backprojected image in figure 16, i.e., a family of ellipsoids with foci along the flight track and its virtual image. Note that the smearing in figure 16 corresponds to a neighbourhood of the intersecting ellipsoids at (50,50) and the corresponding artefact locations.

by a stationary phase analysis of the backprojection in (9), for example. In order to obtain a good reconstruction, the ellipsoids need to intersect at the point in such a way that there is a fairly wide opening angle created by the intersecting ellipses. This angle depends very much on the relative positions of the scatterer and the flight track. This problem is also present for imaging from data sets d_1, d_4 too, but because the ellipsoids can become very elongated when the source is far away from the wall, imaging from d_2, d_3 is intrinsically more difficult.

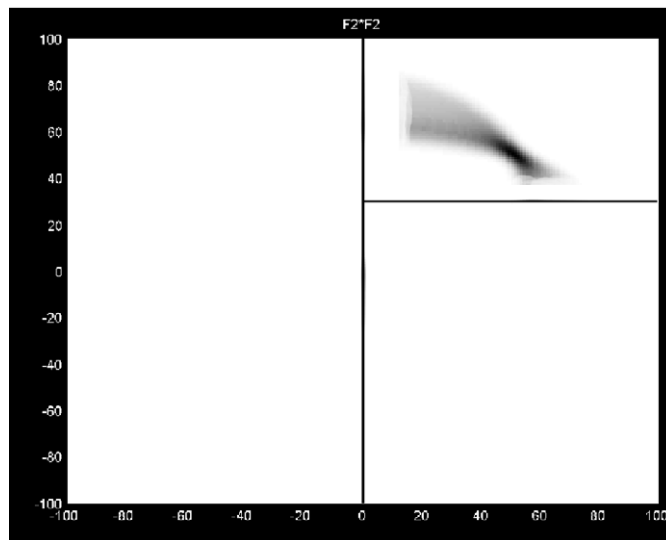


Figure 18. The same reconstruction as in figure 13 but this time with a side-looking radar. This results in the removal of both the ‘left–right’ artefact as well as the artefact situated symmetrically across the wall.

For example, the reconstruction of the point scatterer in figure 14 is not as good as that in figure 16. Ignoring the fact that there are artefacts in both of these images for the moment, the point scatterer is significantly more smeared out in the first quadrant of figure 14 than it is in figure 16. The reason for this can be attributed to the contributing ellipsoids shown in figures 15 and 17, respectively. These ellipsoids were generated using formula (31).

We also point out that figure 14 has extra artefacts which are positioned symmetrically about the wall. In general, these artefacts can be understood using microlocal analysis, but they can also be plainly understood by looking at the intersecting ellipsoids in figure 15. The extra artefacts are similar to the classic left–right ambiguity artefacts discussed above. If we operate a side-looking radar whose footprint lies in only the first quadrant say, then we obtain an artefact-free image, as depicted in figure 18.

5. Conclusions and future work

In conclusion, we have shown how to incorporate a known vertical wall into the background scattering model and how to use this to obtain enhanced angular resolution. Exploiting scattering from the wall gives us more angles of view, and we may be able to see targets from multipath scattering that would not be visible from the conventional Born approximation. We have shown that artefacts can be significantly reduced by correctly exploiting the multipath scattering data.

Finally, if one does not collect data from different scattering paths separately, artefacts will arise from backprojecting data along incorrect paths. The analysis of these artefacts is beyond the scope of this paper and will be dealt with elsewhere.

We also leave for the future the exploration of issues such as handling diffraction and walls made of different materials.

Acknowledgments

TD, RG and CN acknowledge the support of Science Foundation Ireland (Grant 03/IN3/I401). MC acknowledges the support of IPAM and AFOSR (grant FA9550-06-1-0017).

References

- [1] Devaney A J and Dennison M 2003 Inverse scattering in inhomogeneous background media *Inverse Problems* **19** 855–70
- [2] Devaney A J and Guo P 2005 Superresolution imaging from limited-aperture optical diffracted field data *J. Opt. Soc. Am. A* **22** 1086–92
- [3] Morse P and Feshbach H *Methods of Theoretical Physics* vol 1 (New York: McGraw-Hill)
- [4] Nolan C and Cheney M 2003 Synthetic aperture inversion for arbitrary flight paths and non-flat topography *IEEE Trans. Image Process.* **12** 1035–43
- [5] Duistermaat J J 1996 *Fourier Integral Operators* (Cambridge, MA: Birkhauser Boston)
- [6] Cheney M 2001 A mathematical tutorial on synthetic aperture radar *SIAM Rev.* **43** 301–12
- [7] Treves F 1980 *Introduction to Pseudodifferential and Fourier Integral Operators* vols I and II (New York: Plenum)
- [8] Nolan C and Cheney M 2002 Synthetic aperture inversion *Inverse Problems* **18** 221–36
- [9] Nolan C and Cheney M 2004 Microlocal analysis of synthetic aperture radar imaging *J. Fourier Anal. Appl.* **10** 133–48
- [10] Saint X 1991 *Raymond Elementary Introduction to the Theory of Pseudodifferential Operators* (Boca Raton, FL: CRC Press)
- [11] Nolan C J and Symes W W 1997 Global solution of a linearized inverse problem for the wave equation *Commun. PDE* **22** 919–52
- [12] Cheney M and Bonneau R J 2004 Imaging that exploits multipath scattering from point scatterers *Inverse Problems* **20** 1691–711
- [13] Hallberg B, Smith-Jonforsen G and Ulander L M H 2005 Measurements on individual trees using multiple VHF SAR images, geoscience and remote sensing *IEEE Trans.* **43** 2261–9
- [14] Shengli W and Wiesbeck D 1999 The imaging mode of forward looking SAR with two receiving antennas *Geoscience and Remote Sensing Symp. (Hamburg)*